Available online at www.sciencedirect.com

ScienceDirect
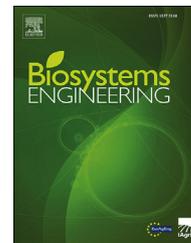
Research Paper

Optimised dispensing of predatory mites by multirotor UAVs in wind: A distribution pattern modelling approach for precision pest management

April L. Teske [a], Gang Chen [a], Christian Nansen [b], Zhaodan Kong [a],*

[a] Department of Mechanical and Aerospace Engineering, University of California Davis, One Shields Avenue, Davis, CA, 95616, USA
[b] Department of Entomology and Nematology, University of California Davis, 367 Briggs Hall, Davis, CA, 95616, USA

Multirotor unmanned aerial vehicles (UAVs), or drones, are increasingly being used to spray liquid pesticides to control emerging pest infestations in field crops. In recent years, UAVs have been used to release predatory mites and other natural enemies to optimise and promote sustainable pest management practices by relying less on conventional insecticides. Drone dispensed samples of predatory mites are typically mixed with a granular material, vermiculite, which serves as a filler. The low density of the vermiculite and weather conditions (mainly wind), influences the distribution pattern of predatory mites when delivered by a UAV-based system. The purpose of this paper is to present a data-driven methodology to develop a mathematical model that can be used to optimise UAV-based autonomous dispensing of predatory mites. The model characterises the distribution of vermiculite as a function of wind speed and direction, and the UAVs altitude and forward speed. The model is constructed by first conducting outdoor experiments and then using machine-learning techniques on the collected data. The constructed model produced an average generalisation error of 12.8%, RMSE. Due to its parametric and predictive nature, the model is amenable for the future design of UAV flight controllers that can compensate for the targeting error caused by wind. The proposed modelling methodology could be useful not only for the dispensing of predatory mites, but also for other UAV dispensing applications, such as liquid or granular pesticide deliveries.

* *Corresponding author.*
    E-mail addresses: atvanhise@ucdavis.edu (A.L. Teske), ggchen@ucdavis.edu (G. Chen), chrnansen@ucdavis.edu (C. Nansen), zdkong@ucdavis.edu (Z. Kong).

1. Introduction

Unmanned aerial vehicles (UAVs), or drones, are revolutionising the field of precision agriculture in a number of important ways. Regarding pest management, UAVs are rapidly replacing manned platforms in two major types of applications. Firstly, due to their relatively low cost and ease of deployment, UAVs are widely used for *remote sensing* (Colomina & Molina, 2014). For instance, they have been used to detect and diagnose abiotic and biotic stress in crops (Nansen & Elliot, 2016), obtain individual tree structure, plant density, parcel boundary area (Rokhmana, 2015), generate georeferenced orthophotos (Bachmann, Herbst, Gebbers, & Hafner, 2013), and determine important crop traits (Gago et al., 2015). Secondly, since UAVs are highly manoeuvrable and can reduce human contact with pest treatment materials such as pesticides, they have been increasingly used for precision chemical application. Since the 1980s helicopter-style UAVs have been used to spray liquid pesticides (Miyahara, 1993; Sato, 2003; Xiongkui, Bonds, Herbst, & Langenakens, 2017). These early pesticide sprayers were normally petrol-powered, manually piloted, and relatively expensive. More recently, a wide range of low-cost, electronic, autonomously controlled multirotor UAVs, such as the DJI AGRAS series, have been developed (Pederi & Cheporniuk, 2015; Ru, Zhou, Fan, & Wu, 2011, p. 1110663; Shim, Han, & Yeo, 2009; Xue, Lan, Sun, Chang, & Hoffmann, 2016; Yun, Mazur, & Pederii, 2017). The rapid technological advancements in both sensing and dispensing using UAVs promises a future where they can work together to enable precise and closed-loop pest management (Fig. 1). Sensing UAVs will scout for pests and identify potential "hot spots", where pest infestations might be emerging; dispensing UAVs will apply necessary treatments, such as pesticides, to the hot spots; the efficacy of the treatment will also be closely monitored by the sensing UAVs for future dispensing adjustment.

The majority of existing dispensing UAVs are developed for liquid pesticide distribution (Filho, Heldens, Kong, & de Lange, 2019). However, in recent years UAV delivery of commercially available natural enemies, such as predatory mites, is gaining momentum and being proposed as a way to optimise the distribution of natural enemies to crops infested with important arthropod pests (Parabug, 2018; Pearl, 2015). An example

that illustrates the potential of UAV-based delivery of natural enemies, the two-spotted spider mites (*Tetranychus urticae*) are considered one of the most important arthropod pests on strawberry as well as a wide range of other crops (Amoah et al., 2016; Howell & Daugovish, 2016). Miticide treatments are very important in spider mite control. However, chemical control of spider mites is often ineffective, as they have developed resistance to around 93 active ingredients (Sparks & Nauen, 2015; Van Leeuwen, Vontas, Tsagkarakou, Dermauw, & Tirry, 2010). In addition, miticide applications adversely affect populations of beneficial natural enemies. Therefore, the use of natural enemies is promoted as being a more effective and environmentally sustainable approach to spider mite management, with the predatory mites (*Phytoseiulus persimilis*, *Neoseiulus californicus*, and *N. fallacis*) being commercially available. Although some companies offer UAV-based delivery, predatory mites are predominantly sprinkled by hand, a process that is both labour intensive and potentially inefficient. Predatory mites have only limited ability to spread and disperse after release. Furthermore, if released where prey populations are low, then the predatory mites will succumb within days. Thus, effective spider mite control with predatory mites is highly influenced by the ability to deliver predatory mites to "hot spots" with emerging spider mite infestations. Such precision delivery is also favourable compared to broadcast dispensing of predatory mites, as this approach to arthropod pest management can be cost-prohibitive on a large scale. One critical link that is still missing to optimise natural enemy dispensing with UAVs is a principled study and explicit modelling of the effects of the wind and flight conditions on the spatial distribution of the dispensed predatory mites. Samples of predatory mites are commercialised and packaged as a mixture with a dry granular lightweight material, vermiculite. Due to the low density of both the predatory mites and vermiculite, factors related to both the wind, e.g., its speed and direction, and the UAV, e.g., its altitude and forward speed, greatly influence the spatial distribution, position and density of the vermiculite and predatory mites being delivered from an airborne UAV. Given the additional fact that the wind changes across regions, terrains, seasons, days, or even seconds (Stull, 2012), without an explicit model to quantify wind effects, precise and repeatable dispensing application with UAVs is unattainable, and that could compromise the performance of this potentially sustainable and innovative approach to pest management.

A similar research problem, i.e., how to quantify the effects of wind and flight conditions on the spray drift from UAV sprayers for liquid pesticides, has been studied. For instance, Qin et al. (2014 & 2016) conducted a series of experiments using a UAV helicopter to spray chemicals onto maize canopies. The authors collected data on the overall distribution uniformity of the liquid droplets within the canopies and then used multi-variable regression to analyse factors, such as wind speed, wind direction, UAV altitude, and UAV speed, on the droplet distribution uniformity. Their model was able to characterise the cumulative distribution of liquid pesticides. But Qin et al. did not model how the distribution may change spatially. The spray distribution is unlikely uniform spatially. If a multi-rotor UAV is used as the dispensing platform (Pederi & Cheporniuk, 2015; Ru et al., 2011, p. 1110663; Shim et al.,
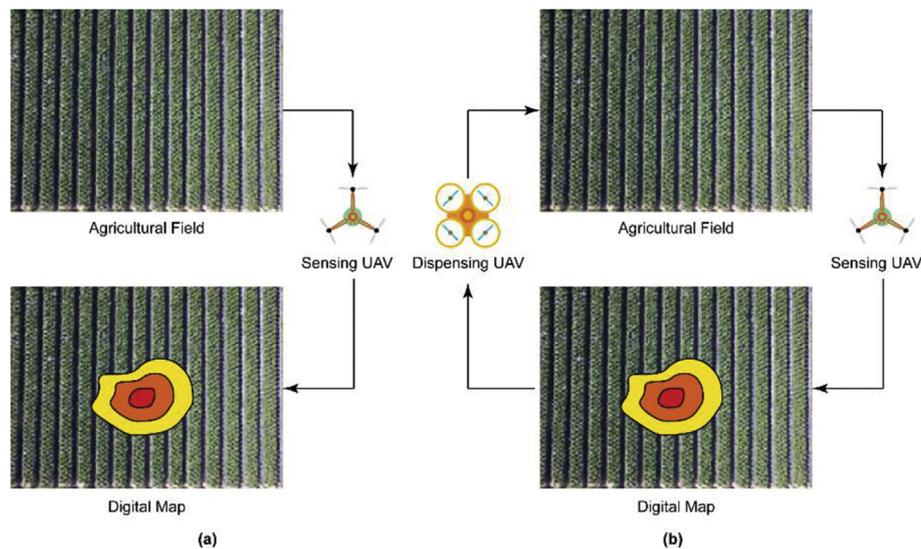
Fig. 1 – **(a) State-of-the-art, open-loop remote sensing paradigm and (b) emerging, closed-loop, integrated pest management paradigm.**

2009; Xue et al., 2016; Yun et al., 2017), even on a windless day, spray densities may vary considerably depending on the distance between the sprayed region and the UAV. Moreover, if wind is present, the downdraft from the UAV rotors will interact with the wind, causing drift and further complicating the spray distribution pattern. How to precisely and explicitly model a fine-grained spatial distribution of pest treatments, particularly predatory mites as a function of wind and flight conditions, is still an open problem.

In this paper, we develop a model to predict the spatial distribution of a granular material, vermiculite, as a function of wind speed and direction, and UAV altitude and speed. It is assumed that distribution of predatory mites is proportional to that of the vermiculite. Therefore, the model also characterises how the distribution of the predatory mites might change with the various aforementioned wind and flight conditions. To develop such a model, a series of outdoor experiments were designed and conducted where vermiculite was dispensed using a multi-rotor UAV. For each flight mission, data were collected regarding the UAV altitude and speed as well as wind speed and direction, and the quantified spatial distribution of vermiculite. Subsequently, machine-learning techniques, such as feature selection, were applied to train a model that maps the wind and flight conditions to the vermiculite spatial distribution. Finally, the predictive power and the physical meaning of the model were evaluated.

Although this paper focuses on dispensing predatory mites with a multi-rotor UAV, the experimental design and computational methods presented in this paper have significant implications and relevance to other agricultural applications, in which UAVs are needed for the purposes of dispensing material. Moreover, the model developed is amenable to the principled design of a flight controller for the multi-rotor UAV, which can predict the effects of the wind and compensate for the effects, thus enabling precise dispensing. UAVs with such capabilities will continue to prove important as solutions to emerging challenges and to face demands for more efficient

and sustainable agricultural practices. From an engineering standpoint, this study highlights important aspects of how to optimise the closed-loop system as shown in Fig. 1.

2.   Materials and methods

2.1.   Experiment hardware

The UAV used in our experiments was a DJI S1000 + octocopter (DJI, Shenzhen, China) equipped with a DJI A3 Pro flight controller and a DJI Lightbridge 2 radio controller (Fig. 2). This UAV was chosen for its high payload capability. The UAV flight path can be programmed using waypoints within an app called Litchi (Litchi, 2018), which was run on an iPad (Apple, Cupertino, CA, USA). Litchi was able to record the onboard flight data and synchronise them to the Airdata UAV website (Airdata UAV, 2018), where flight data, such as UAV speed and altitude, can be downloaded as a CSV file.


Fig. 2 – **The DJI S1000 + octocopter used in our experiments. The vermiculite dispenser, called "Bugbot" (see Fig. 4), was attached to the bottom of the UAV.**

Wind speed and direction were measured and recorded with a commercial anemometer and wind vane - the Onset U30 Hobo Weather Station (Onset Computer Corporation, Bourne, MA, USA) The sampling frequency of the weather station was set to 3 Hz. Due to the difference between the true north and the magnetic north (Beard & McLain, 2012), the measured wind direction was corrected first as follows. The UAV heading and flight path were provided with waypoints on a map in Litchi. The UAV heading was at an angle of 95° from true north. A magnetic declination of 13.5° East was determined at our experiment location using the World Magnetic Model on the U.S. National Oceanic and Atmospheric Administration (NOAA) website, https://www.ngdc.noaa.gov/geomag/declination.shtml. This declination value was subtracted from 95° true north to calculate a UAV heading of 81.5° from magnetic north. The wind direction was measured as the degree from which the wind originated. Since the vermiculite distribution depends on the relative wind direction with respect to the UAV heading, thus the measured wind direction was converted to a representation with respect to the UAV heading as shown in Fig. 3.

The vermiculite dispenser used in our experiments was dubbed the "Bugbot dispenser". It was a 3D printed custom designed plastic device which consisted of a 3.5-litre funnel-shaped container and a feeder with a paddle wheel that dispensed the vermiculite (see Fig. 4 for the Bugbot design and Fig. 2 for a picture of the Bugbot attached to a DJI UAV). The paddle wheel was powered by a continuously rotating servo motor, which was controlled by an Arduino Uno (Arduino, Ivrea, Italy) and turned on and off remotely through the shutter button on the UAV radio controller.

2.2. Outdoor experiment setup

A series of outdoor experiments were conducted from May through to August 2018 in Davis, California. The testing field was a paved road pointing east-west in the middle of a grassy field, with no buildings or trees nearby (Figs. 6b and 7). The UAV was flown along the paved road over two rows of 0.6-m
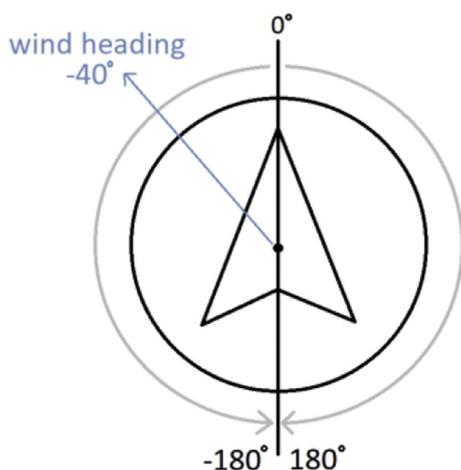
Fig. 3 — Wind direction representation. The UAV heading is defined as 0°. If the wind direction is to the left of the UAV heading, it is negative; if it is to the right of the UAV heading, it is positive.

square boards of plywood that were arranged perpendicular to the flight path (Fig. 6a). Each board was covered with a large roll of carpet protection tape with the adhesive side facing upwards, and they were secured to the boards with large binder clips. Each board was raised on concrete cinder blocks in order to obtain a representative cross section of the vermiculite drop (Fig. 6b). The elevation of the boards was important as it allowed the avoidance of cross contamination from any vermiculite accumulation on the ground. The adhesive boards collected the vermiculite as it was dispensed from the UAV.

Flight missions were performed by the UAV using three different ground speeds: 1.8 km h^{-1}, 4.0 km h^{-1}, and 8.2 km h^{-1}; and two different altitudes: 2.7 m and 3.7 m. These speeds and altitudes were chosen to collect data that would be relevant to strawberry fields in which plants are arranged in beds 1—1.5 m wide. The Bugbot dispenser was operated with a constant flow rate of 4.7 g [vermiculite] s^{-1}. Each combination of UAV speed and height was tested under a minimum of two different wind conditions. Days with steady, or consistent, forecasted wind conditions were chosen for testing. Also, each day of testing was chosen to cover a range of different wind speeds and directions. A video clip showing one such flight mission can be found at https://youtu.be/z4kM_9KdLDs. A total of 14 missions were conducted.

The configuration of boards with adhesive surface was a 2 by 8 grid (Fig. 6(a)). After each flight mission, the adhesive surface was cut into four sample squares, resulting in 16 columns (perpendicular to the UAV flight path, defined as the X-axis) and 4 rows (along the UAV flight path, defined as the Y-axis). A position to the left of the flight path was defined as having a negative x coordinate, while that to the right was defined as a positive x coordinate (Fig. 6a).

The reported horizontal accuracy of the Global Positioning System (GPS) unit on the UAV was about 1.5 m. To account for this error, each flight was recorded by a video camera, which was placed near the take-off point of the UAV. A person on the side of the field gave a visual cue to the camera when the UAV reached each row of boards (Fig. 7). During playback of the video, the UAV alignment across the row of 16 squares was observed and rounded to 0.15 m. A timestamp of the UAV arrival at each row of boards was also recorded. All clocks on the weather station, iPad, and smart phone timer were synchronised to the second (Fig. 5).

2.3. Vermiculite density calculation

After each flight mission, a piece of newsprint paper was placed on top of each adhesive surface, so that the vermiculite was secured between the adhesive plastic and newsprint paper. Each corner of the large sample was labelled, and the large sample was cut into four smaller samples (Fig. 8a). Each square was imaged individually on a light table. The transparency of the newsprint paper allowed the light from the imaging light board to illuminate the empty space around the vermiculite (Fig. 8b). The vermiculite showed up as dark dots in contrast to the background. Next, the image taken was analysed using ImageJ software (ImageJ, 2018). Specifically, the images went through a series of steps where they were stacked, changed to black and white, cropped, analysed for
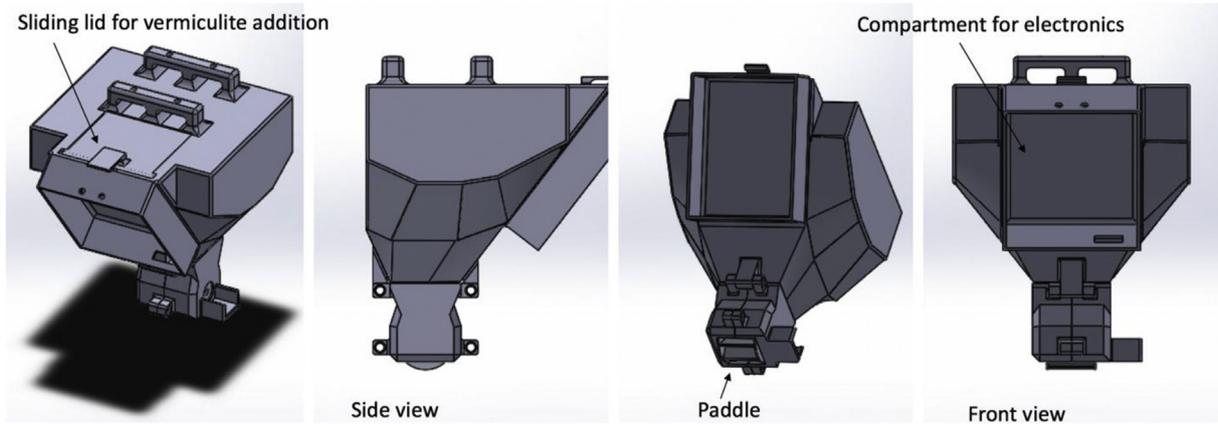
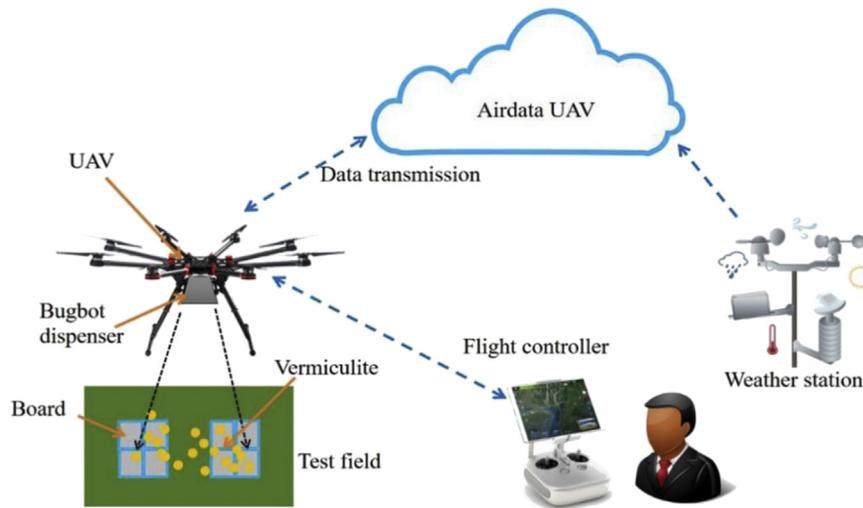Fig. 4 – CAD drawing of our Bugbot dispenser design.
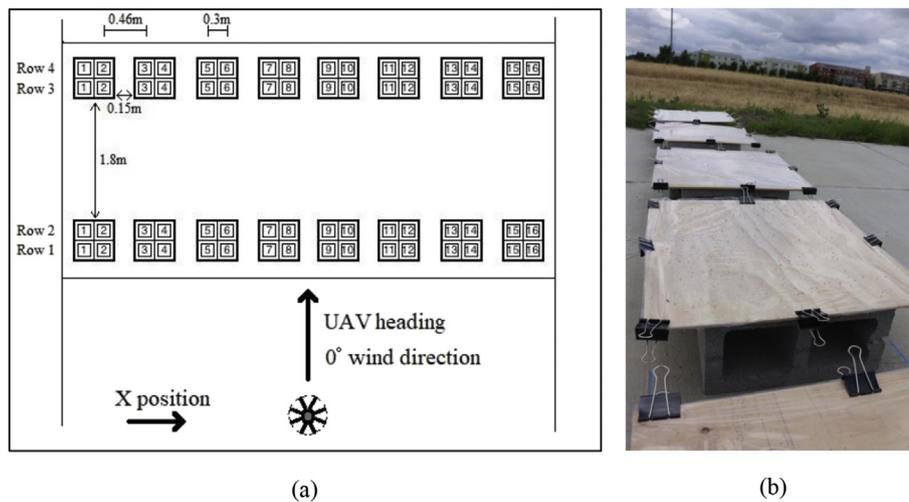

Fig. 5 – Data collection framework.

(a)   (b)

Fig. 6 – Experiment field layout: a) Each large square is a 0.6 by 0.6 m board; b) Boards with adhesive tapes.

Fig. 7 — Procedure taken to correct for GPS error. A timestamp and a visual cue were recorded when the UAV reached a row of boards.

particle size, and finally condensed into the total area of the dark space in each sample.

In order to quantify the weight and subsequently the density of vermiculite on each square of adhesive surface, a calibration experiment was performed to correlate the imaged dark area to vermiculite weight. Specifically, three duplicate calibration squares were created by weighing out known amounts of vermiculite and carefully pouring it by hand onto separate clean squares of adhesive material, keeping all weighed vermiculite within the marked area that would be captured by the imaging camera. Then a piece of newsprint paper was placed on top to emulate the sampling process. The calibration squares were made for a series of weights: 0.010 g, 0.025 g, 0.050 g, 0.100 g, 0.200 g, and 0.300 g. The largest calibration weight, 0.300 g, was chosen to allow its equivalent density, 7.27 g m^{-2}, exceeding the maximum vermiculite density value obtained from the experiments, which was 4.95 g m^{-2}. The calibration squares were used to linearly fit the vermiculite density with the total dark area as shown in Fig. 9. The regression line was forced through zero and the resulting calibration curve had an R^2-value = 0.9992. The fitted equation

(see Fig. 9 caption) was used to convert measured total dark area, as obtained from ImageJ analysis of the adhesive boards, into estimates of vermiculite density.

3. Results and discussions

### 3.1. Data-driven vermiculite density modelling

The outdoor data collections (section 2.2) and vermiculite density calculations (section 2.3) resulted in a data set that consisted of 14 flight missions, each comprising four rows of vermiculite density data (see Fig. 6a). However, because the wind conditions were non-constant among rows, only the two rows residing on the same physical board were considered replicates of each other and combined into one observation. For instance, in each flight mission rows 1 and 2 were replicates of each other, with the same exact recorded wind and UAV conditions. Therefore, rows 1 and 2 together were considered one observation. With each flight mission
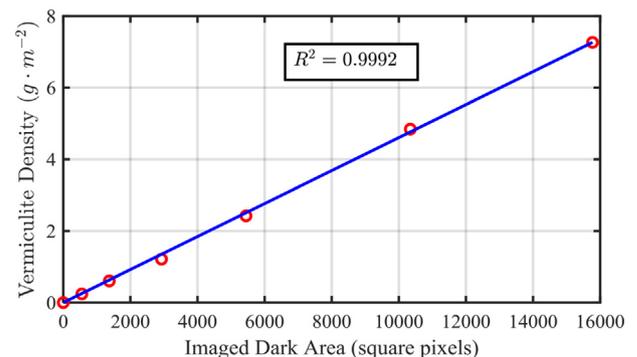
Fig. 9 — Linear regression curve for the conversion of imaged dark area (in square pixels) to vermiculite density (in g m^{-2}). The calibration equation is *Vermiculite Density* = 0.0428 × *Imaged Dark Area*.

(a)
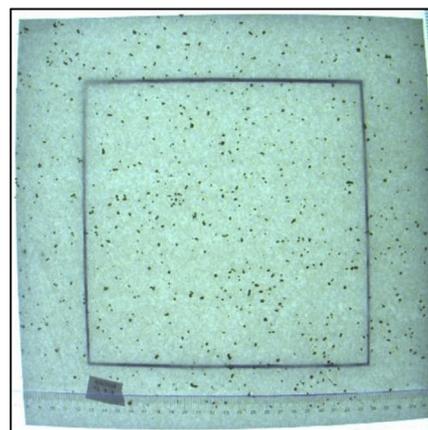
(b)

Fig. 8 — a) Large sample was cut into four smaller sample squares. b) Each smaller sample square was imaged individually on a light board. The vermiculite showed up as dark dots in contrast to the background when placed on a light table.

producing two sets of observations, the entire experiment resulted in 28 total observations (Fig. 10).

To develop a mathematical model based on the collected data, letting ρ be vermiculite density (in g m^{-2}), x the X coordinate (in m), h the UAV altitude (in m), v the UAV forward speed (km h^{-1}), w_x and w_y the wind speed in the X direction and flight path directions (both in km h^{-1}) respectively. ($w_x = w\sin(\alpha)$ and $w_y = w\cos(\alpha)$ with w being the magnitude of the wind speed and α being the direction of the wind in degrees.) Given a combination of h, v, w_x and w_y, the model should prescribe $\rho(x)$, ρ as a function of x or the vermiculite density for any x position. Provided with a target vermiculite distribution and the current wind condition, a UAV can then use such a model to compute its desired speed and altitude to achieve precision dispensing. Supervised machine learning, specifically nonlinear regression, was used to train such a model (Alpaydin, 2010). Nonlinear regression searches for essential patterns that can map an input, e.g., a combination of h, v, w_x and w_y, to an output, e.g., ρ, and learns a model that is simple but still with enough generalisation capability. Specifically, the model was derived in two major steps. Firstly, the functional form between the vermiculite density and X position was selected (section 3.1.1) and secondly the coefficients of the functional form selected in the first step were determined via feature selection and cross-validation (section 3.1.2).

3.1.1.   Functional form selection

When the vermiculite density was plotted against the X position, a consistent Gaussian-shape was observed (Fig. 10). Consequently, we chose to model the functional relationship between the vermiculite density ρ and x position by an exponential functional form as follows:

$$\rho = e^{a_0 + a_1 x \cdots, + a_n x^n} \tag{1}$$

where a_i, $i = 0, …, n$ are the coefficients of the exponent and n is the order of the polynomial function.

To determine n, the order of the polynomial function, we examined R^2, the coefficient of determination, for different orders and all 28 observations (Fig. 11). The R^2 value indicates the amount of variation in the dependent variable, ρ, that is attributable to the variation in the independent variable, x. An R^2 value closer to one is desirable as it denotes a stronger correlation between the two variables, whereas values closer to zero signify a lack of relationship (Wood & Henry, 2011). According to Fig. 11, the second and third order polynomials
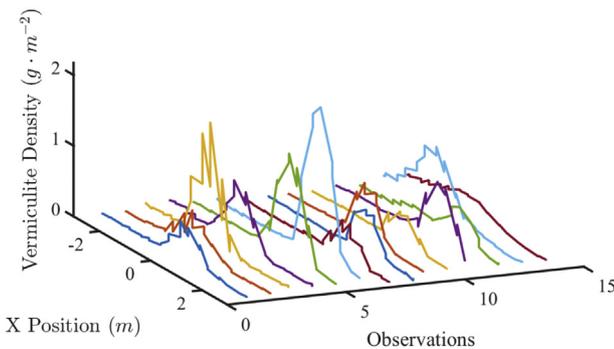
Fig. 10 – Raw data of vermiculite density versus x position for 14 observations (half of collected data).

both provide sufficient R^2 values. The difference between the two is negligible. Therefore, the simpler second order polynomial was selected and then Eq. (1) becomes:

$$\rho = e^{a_0 + a_1 x + a_2 x^2} \tag{2}$$

An exponential model with a second order polynomial as its exponent can be re-formulated as a Gaussian functional form:

$$\rho = e^{b + \lambda(x - \mu)^2} \tag{3}$$

where b is the bias, λ is the variance, and μ is the mean of the Gaussian curves graphed by x and ρ (Guo, 2011).

3.1.2.   Coefficient determination

The resulting Gaussian functional form, Eq. (3), is characterised by three undetermined coefficients: the bias b, the variance λ, and the mean μ. Therefore, the logical next step is to determine the specific functions of these coefficients, i.e., the relationships between the coefficients and the experiment conditions, specified by four parameters: UAV altitude (h), UAV speed (v), wind speed in the X direction (w_x), and wind speed along the flight path (w_y). Nonlinear regression was used, together with feature selection (Alpaydin, 2010), to determine these relationships (coefficient functions). It was assumed each of the coefficients, b, λ, and μ, can be modelled as a linear combination of a properly selected feature vector constructed from the four parameters, i.e.,

$$b = f_1(p_1), \ \lambda = f_2(p_2), \ \mu = f_3(p_3) \tag{4}$$

where f_i, $i = 1, 2, 3$, is a linear function and p_i, $i = 1, 2, 3$, is a feature vector. The key then was to determine p_i. To achieve this, a set of features were constructed with different orders as follows:

First order features:

$$\Gamma_1 = \begin{bmatrix} h, v, w_x, w_y \end{bmatrix}$$

Second order features:

$$\Gamma_2 = \begin{bmatrix} h, v, w_x, w_y, h^2, \ hv, hw_x, hw_y, v^2, \ vw_x, vw_y, w_x^2, \ w_x w_y, w_y^2 \end{bmatrix}$$

Third order features:

$$\Gamma_3 = \begin{bmatrix} h, v, w_x, w_y, h^2, \ hv, hw_x, hw_y, v^2, \ vw_x, vw_y, w_x^2, \ w_x w_y, w_y^2, \\ h^3, h^2 v, h^2 w_x, h^2 w_y, v^3, \ v^2 h, v^2 w_x, v^2 w_y, \\ w_x^3, w_x^2 h, w_x^2 v, w_x^2 w_y, w_y^3, \ w_y^2 h, w_y^2 v, w_y^2 w_x \end{bmatrix}$$

Then a standard forward feature selection algorithm together with four-fold cross-validation (Alpaydin, 2010; Hastie, Tibshirani, & Friedman, 2009) were executed to select the optimal order and feature vector for each coefficient (see Eq. (4)). Specifically, the algorithm added one feature at a time to the feature vector based on the p-value. The p-value was calculated based on the linear regression performance for that particular feature. To avoid over-fitting, a four-fold cross-validation process was conducted, since four-fold had better performance than three, five, or six-fold experimentally. The entire data set was broken down randomly into four equal sections; one section was left as the testing data, while the other three sections were used as the training data for the
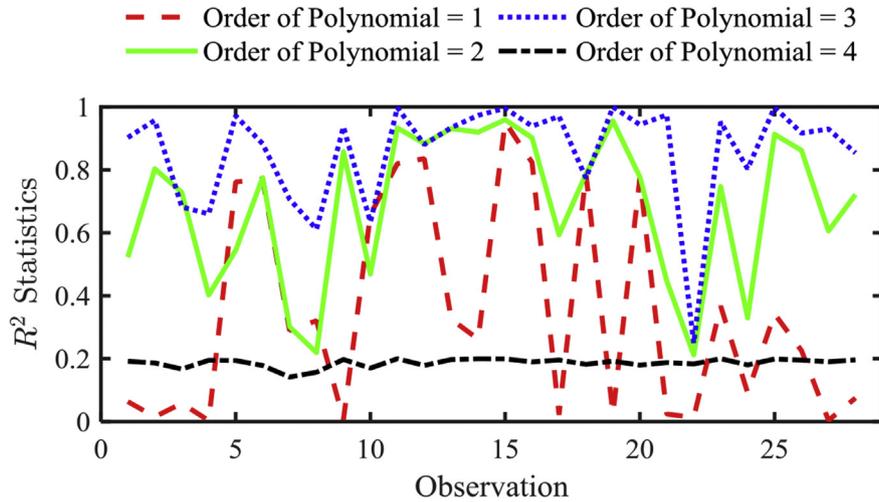
Fig. 11 – R^2 value per observation for different orders (n in Eqn. (1)) of the polynomial function.

linear regression; this procedure was repeated four times so that each section served as the testing data for the other sections once. The generalisation error, defined as the root mean squared error (RMSE) in this paper, was then calculated and used to select the feature that would be added to the feature vector. The described feature selection algorithm was run 20 times due to the random nature of the cross-validation process. The entire coefficient determination process is summarised in Algorithm 1.

Algorithm 1. Coefficient Determination.

After implementing Algorithm 1, the mean generalisation errors and their corresponding variances were calculated for each possible number of features (we chose T the maximum number of features as 10) and for each of the three coefficients, b, λ, and μ, as shown in Fig. 12, which were the results of 20 runs of Algorithm 1. It can be observed that the generalisation error of the second order features did not differ significantly from that of the third order. Therefore, the feature vector for each coefficient, b, λ, and μ was constructed from the second order feature set Γ_2.

Input: The experimental data set D, feature sets Γ_1, Γ_2, and Γ_3, and the maximum number of features T.

Output: Functions of bias b, variance λ, and mean μ

/*Given an experiment condition, parametrised by a vector $p = [h, v, w_x, w_y]'$, these functions should be able to predict the exact values of b, λ, and μ, which together should be able to predict the exact vermiculite distribution function $\rho(x)$.*/

0: For b

/*The exact same procedure can be used for λ and μ, since the functions of b, λ, and μ are learned independently.*/

1: Set Γ to an empty set;

2: **For** $i = 1{:}3$ **do**

3:     **For** $j = 0{:}\#(\Gamma_i)$ with $\#(\Gamma_i)$ being the number of features in Γ_i **do**
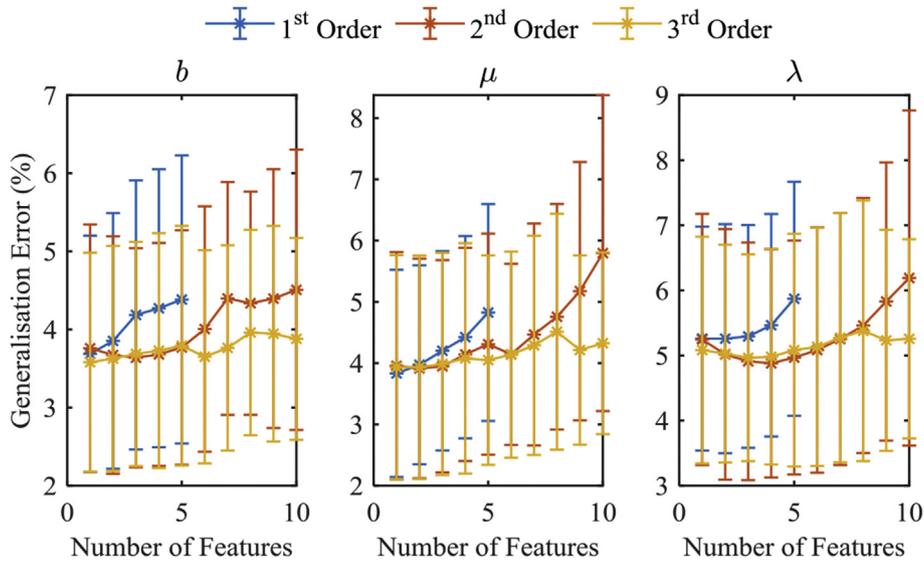
4:         Take a feature $\gamma_{i,j}$ from Γ_i and add $\gamma_{i,j}$ to Γ to get $\Gamma_{i,j} = [\Gamma, \gamma_{i,j}]$;

5:         Use cross-validation to select the best γ^* from all $\gamma_{i,j}$ in Γ_i;

/*The criterion used for selecting the best feature is the RMSE of b as a linear combination of all the features in $\Gamma_{i,j}$.*/

6:         Remove γ^* from Γ_i and add it to Γ;

7:         **Stop** if $\#(\Gamma) \geq T$ with $\#(\Gamma)$ being the number of features in Γ.

Fig. 12 – Generalisation error versus model complexity for each of the three Gaussian coefficients b, λ, and μ (with error bars shown). Blue lines: first order features only; Orange lines: first and second order features; Yellow lines: first, second, and third order features.

3.1.3. Learned mathematical model

The learned functions of the Gaussian coefficients (see Eq. (4)) are as follows:

$$b = -2.620 - 0.3347v - 0.2082w_y + 0.5677hv \quad (5)$$

$$\mu = -0.1715 - 0.1658w_x - 0.9565hw_x \quad (6)$$

$$\lambda = -30.59 - 44.96h - 7.377v + 138.1hw_y + 1.502vw_y \quad (7)$$

These three functions, together with Eq. (3), constitute our finalised vermiculite distribution model:

$$\rho = e^{\left(-2.620 - 0.3347v - 0.2082w_y + 0.5677hv\right)} *$$
$$e^{\left(-30.59 - 44.96h - 7.377v + 138.1hw_y + 1.502vw_y\right)\left(x + 0.1715 + 0.1658w_x + 0.9565hw_x\right)^2} \quad (8)$$

The averaged generalisation error, quantified by RMSE, of our mathematical model over the entire data set is 12.8%. It is worth pointing out that turbulence is an intrinsic part of the atmospheric boundary layer (the lowest 100–3000 m of the atmosphere) (Luce, Kantha, Hashiguchi, Lawrence, & Doddi, 2018; Stull, 2012). Therefore, a 12.8% error is satisfactory considering the random nature of turbulences, which is a significant confounding factor in any outdoor flight mission. Two examples of the real vermiculite density data versus the density predicted by our model are shown in Fig. 13. Together with the low generalisation error, they illustrate that our mathematical model presents a good approximation of the real experimental data.

3.2. Interpretations of Gaussian coefficients

To understand the results of the final model with respect to real life situations, parameters are fed into the model and the resulting predicted distributions are analysed. Specifically, how wind conditions, such as wind speed, w, and wind direction, α, and flight conditions, such as UAV altitude, h, and UAV speed, v, affect the three Gaussian coefficients, bias, b, mean, μ, and variance, λ, was explored.

3.2.1. Bias b or peak amplitude

The amplitude of the Gaussian peak can be represented by a coefficient, A, which is related to the bias, b, as follows:

$$A = e^b \quad (9)$$

This gives a different form of the Gaussian function (Eq. (3)):

$$\rho = e^{b + \lambda(x - \mu)^2} = e^b e^{\lambda(x - \mu)^2} = Ae^{\lambda(x - \mu)^2} \quad (10)$$

The amplitude, A, is directly proportional to the height of the peak. According to Eq. (5), the bias, b, depends on three parameters: h, the UAV altitude, v, the UAV speed, and w_y, the wind speed along the flight path.

Figure 14 shows the Gaussian functions with respect to two different UAV altitudes if no wind is present. It can be observed that a lower altitude results in a slightly lower and wider peak. One possible explanation is that, when the UAV is flying at a lower altitude, the downdraft from its rotors deflects off the ground, creating the "ground effects" (Chan, Wei, Lee, & Kong, 2019; Milluzzo & Leishman, 2010). The downdraft from a rotor near the ground was blocked by the opposite downdraft from the other rotors. The blockage creates a recirculation between multi-rotors so that the exit velocity in the control volume is reduced. This recirculation and disturbance of flows are considered as the interactional aerodynamics between multiple rotor wakes, resulting in a wider spread of vermiculite.

In order to evaluate the dispensation effectiveness, for Fig. 14 (as well as Figs. 15–18), the areas under the Gaussian curves were calculated. The area can be considered as the accumulative vermiculite density along the X direction, the direction perpendicular to the flight path. The larger the area,
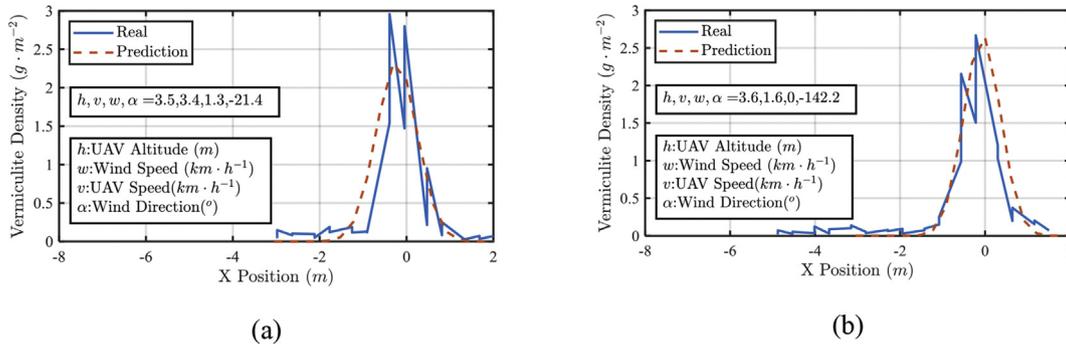
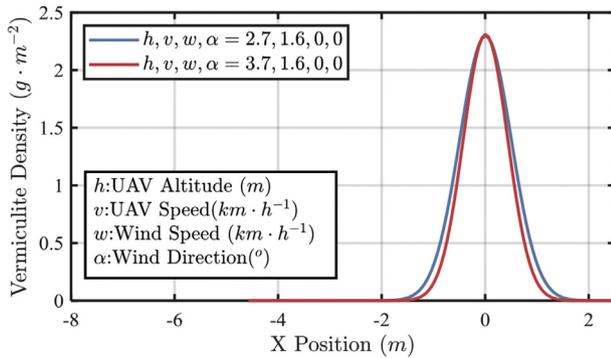Fig. 13 − Comparison of real vermiculite density data and density predicted by our mathematical model.

Fig. 14 − The effects of UAV altitude on vermiculite distribution, when there is no wind. The areas under the blue and red curves (in g m^{-1}) are 879 and 759, respectively.

will be released along the path, and the higher the peak of the Gaussian curve, and the larger the area under the curve. All these results are quite intuitive.

Finally, wind direction can also greatly affect the vermiculite distribution pattern as shown in Fig. 16. If the wind direction is at zero degree, or a tailwind to the UAV, the peak is shorter and wider than those resulting from a −90 or 90° wind (i.e., a lateral wind) and the total area under the curve is largest. In the case where the UAV experiences a headwind, a wind in the 180° or −180° direction, the peak becomes higher and narrower than the peaks of −90° and 90° winds and the area under the curve is smallest. One possible explanation for such observations is as follows. If the UAV is flying in a headwind, once the vermiculite is released and the wind starts to exert a force on the vermiculite, the vermiculite moves in a direction opposite to the UAV's flying direction and exits the downdraft from the UAV, which eventually reduces the spread in the X direction. In contrast, if the UAV is flying in a tailwind, the vermiculite will be pushed in the same direction that the UAV is flying, and as it experiences downdraft from the UAV, will be further dispersed in the X direction. Figure 16 also shows that a lateral wind (a −90° or 90° wind) shifts the position of the peak in the X direction, as expected. All these observations illustrate that wind can shift and change the shape of the vermiculite distribution substantially. A wind of 1.6 km h^{-1} can shift the peak by almost 1 m. Such effects due to the wind, if not accounted for, will dramatically

the more vermiculite dispensed per unit of UAV forward displacement. The calculated areas under the two Gaussian curves (see the caption of Fig. 14) show that when the UAV flies at the higher altitude of 3.7 m, the resulting area is lower than that of the 2.7 m. This indicates the possibility that some vermiculite is being lost and carried off the target area.

The bias b also depends on the UAV speed as shown in Fig. 15. The slower the UAV speed, the more total vermiculite
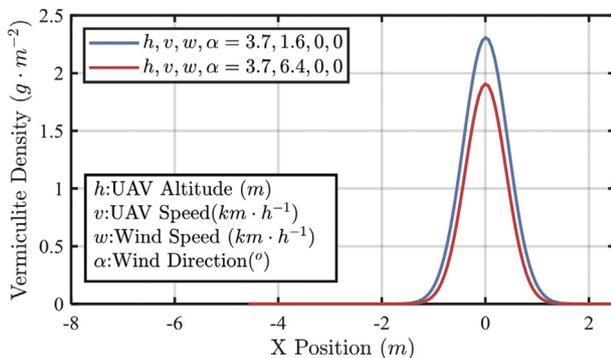

Fig. 15 − The effects of UAV speed on vermiculite distribution, with no wind. The areas under the blue and red curves (in g m^{-1}) are 759 and 574, respectively.
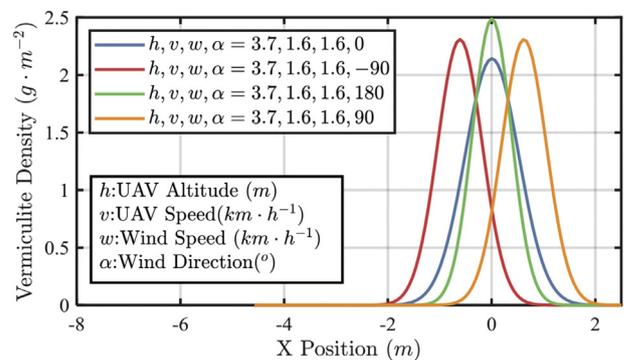

Fig. 16 − The effects of wind direction on vermiculite distribution. The areas under the blue, red, green, and orange curves (in g m^{-1}) are 850, 759, 714, and 759, respectively.

degrade the vermiculite (and subsequently predatory mites) dispensation efficiency and effectiveness.

3.2.2. Mean μ or peak shift

According to Eq. (6), the mean, μ, which characterises the peak shift, depends on two parameters: h, the UAV altitude, and w_x, the wind speed in the X direction. As shown in Fig. 17, w_x affects the X position of the peak. The larger the wind speed, the further the peak will shift away from the UAV flight path. The fact that the area of the peaks is the same for all wind speeds indicates that the lateral winds do not affect the overall amount of the dispensed vermiculite. As shown in Fig. 18, the UAV altitude also affects the peak shift during a lateral wind. The higher the UAV altitude, the longer the vermiculite must travel through the air to reach the ground and the farther the peak will shift away from the flight path.

3.2.3. Variance λ or peak width

According to Eq. (7), the variance, λ, which characterises the width of the peak, depends on three parameters: h, the UAV altitude, v, the UAV speed, and w_y, the wind speed along the flight path. As previously shown, lower UAV altitude (Fig. 14) or lower UAV speed (Fig. 15) widens the peak. Moreover, when all the parameters except the wind direction are kept the same, the peak is widest at zero degrees, and the width decreases as the magnitude of the angle increases, until it reaches 180° which produces the narrowest peak (Fig. 16).

3.3. Implications to precision dispensing and flight controller design

All the results presented so far, based on either our experiment data or vermiculite distribution model, point to the fact that the wind and flight conditions can significantly affect the vermiculite (and thus predatory mites) distribution pattern. Without considering such effects, precise, autonomous vermiculite dispensation with UAVs is unattainable. For instance, assume the scenario that a UAV equipped with a dispenser, such as the Bugbot, is tasked to dispense vermiculite mixed with predatory mites for the treatment of the two-spotted spider mite in rows of strawberry crops. Additionally, it was assumed that an infested row has been detected (by a
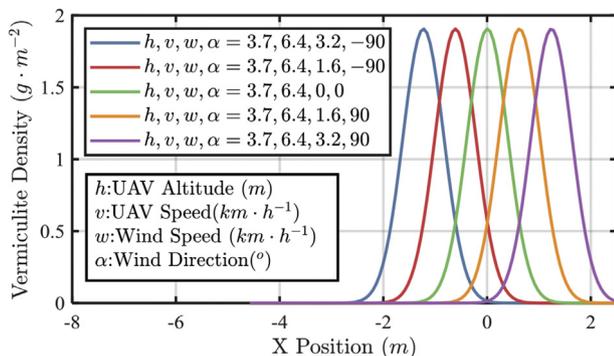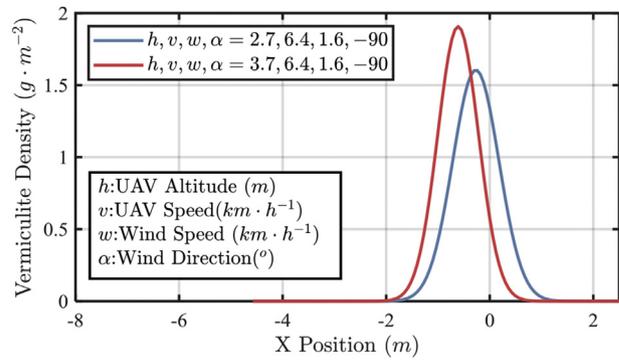
Fig. 18 – The effects of UAV altitude on vermiculite distribution, during a lateral wind. The areas under the blue and red curves (in g m⁻¹) are 548 and 575, respectively.

sensing UAV as shown in Fig. 1, for instance) and that a strong lateral wind (perpendicular to the row direction) is present. If the UAV was pre-programmed to fly along and above the row, two undesirable consequences may happen. Firstly, the amount of dispensed predatory mites may either exceed or be below the necessary dose, thus degrading treatment efficiency. Secondly, the dispensed predatory mites might completely miss the target due to the wind, resulting in ineffectiveness.

Both of these undesirable consequences may be mitigated by incorporating our mathematical model into the design of a flight controller. The basic concept is based on the measured wind condition, target position, and the required amount of mites, the model allows the controller to back-calculate the required UAV speed, position, and altitude, and then steer the UAV to the required speed, position, and altitude. There are a number of ways such a controller could be designed. For instance, Faical et al. (2014 & 2016) and Costa et al. (2012) showed in simulation that a liquid pesticide distribution model could be utilised to control an autonomous UAV to accurately target rows of crops. Their controller used particle swarm optimisation (PSO) to adjust the path of the UAV for precise spraying of liquid pesticides in dynamically varying weather conditions. Another option is to adopt the widely used model predictive controller (Borrelli, Bemporad, & Morari, 2017; Mettler, Dadkhah, & Kong, 2010; Mettler, Kong, Goerzen, & Whalley, 2014), which is a research effort we are currently undertaking.

4. Conclusion

Wind conditions and UAV downdraft can affect the delivery and distribution patterns of natural enemies, including predatory mites. Thus, effective UAV-based delivery of natural enemies to infested hot spots in crop fields will require some level of model-based correction. The main purpose of this study was to develop a model that can predict the distribution of pest treatment and then be used to provide optimised autonomy for better targeting of UAV-based delivery of natural enemies. Outdoor experiments were performed to provide data of the spatial distribution of pest treatment as dispensed

Fig. 17 – The combined effects of wind speed and direction on vermiculite distribution. The areas under the blue, red, green, orange, and purple curves (in g m⁻¹) are the same, which is 574.

from a multirotor UAV, under different wind and UAV conditions. The data was used to train a vermiculite distribution model using supervised machine learning techniques. The model demonstrated that: 1) it is possible to predict vermiculite distribution density with a high level of accuracy (an average 12.8% generalisation error), and 2) parameterisation of effects of wind and flight conditions on the vermiculite distribution pattern can be used to optimise UAV-based delivery of natural enemies. Even though the model was developed for delivery of vermiculite mixed with predatory mites, our experiment and modelling methodology can be readily adopted by other research efforts, where UAVs are used to dispense and/or deliver other treatments as part of UAV-based precision agriculture.

Acknowledgements

R E F E R E N C E S

Airdata UAV. Retrieved on https://airdata.com/, (2018)–. (Accessed 7 October 2018).

Alpaydin, E. (2010). *Introduction to machine learning* (2nd ed.). Cambridge, MA: MIT Press.

Amoah, B., Anderson, J., Erram, D., Gomez, J., Harris, A., Kivett, J., et al. (2016). Plant spatial distribution and predator–prey ratio affect biological control of the twospotted spider mite Tetranychus urticae (Acari: Tetranychidae) by the predatory mite Phytoseiulus persimilis (Acari: Phytoseiidae). *Biocontrol Science and Technology, 26*(4), 548–561.

Bachmann, F., Herbst, R., Gebbers, R., & Hafner, V. V. (2013). Micro UAV based georeferenced orthophoto generation in VIS+ NIR for precision agriculture. *ISPRS-International Archives of the Photogrammetry, Remote Sensing and Spatial Information Sciences*, 11–16. XL-1/W2.

Beard, R. W., & McLain, T. W. (2012). *Small unmanned aircraft: Theory and practice.* Princeton, NJ: Princeton University Press.

Borrelli, F., Bemporad, A., & Morari, M. (2017). *Predictive control for linear and hybrid systems.* New York, NY: Cambridge University Press.

Chan, S. N., Wei, P., Lee, S., & Kong, Z. (2019). Mitigating ground effect on mini quadcopters with model reference adaptive control. *Journal of Intelligent and Robotic Systems, 3*(3), 283–297.

Colomina, I., & Molina, P. (2014). Unmanned aerial systems for photogrammetry and remote sensing: A review. *ISPRS Journal of Photogrammetry and Remote Sensing, 92*, 79–97.

Costa, F. G., Ueyama, J., Braun, T., Pessin, G., Osório, F. S., & Vargas, P. A. (2012). The use of unmanned aerial vehicles and wireless sensor network in agricultural applications. In *2012 IEEE International geoscience and remote sensing symposium* (pp. 5045–5048).

Faical, B. S., Pessin, G., Filho, G. P. R., Carvalho, A., Furquim, G., & Ueyama, J. (2014). Fine-tuning of UAV control rules for spraying pesticides on crop fields. In *2014 IEEE 26th International Conference on tools with artificial Intelligence* (pp. 527–533).

Faical, B. S., Ueyama, J., & Carvalho, A. (2016). The use of autonomous UAVs to improve pesticide application in crop fields. In *2016 17th IEEE International Conference on mobile data management (MDM)* (Vol. 2, pp. 32–33).

Filho, F. H., Heldens, W. B., Kong, Z., & de Lange, E. S. (2019). *Drones: Innovative technology for use in precision pest management.* Entomologia Experimentalis et Applicata (In press).

Gago, J., Douthe, C., Coopman, R., Gallego, P., Ribas-Carbo, M., Flexas, J., et al. (2015). UAVs challenge to assess water stress for sustainable agriculture. *Agricultural Water Management, 153*, 9–19.

Guo, H. (2011). A simple algorithm for fitting a Gaussian function. *IEEE Signal Processing Magazine, 28*, 134–137.

Hastie, T., Tibshirani, R., & Friedman, J. (2009). *The elements of statistical learning: Data mining, inference, and prediction* (2nd ed.). New York, NY: Springer.

Howell, A. D., & Daugovish, O. (2016). Biocontrol of spider mites in California strawberry production. *International Journal of Fruit Science, 16*(sup1), 169–177.

ImageJ. (2018). Software from. http://imagej.nih.gov/. (Accessed 7 October 2018).

Litchi. (2018). App. From. https://flylitchi.com/. (Accessed 7 October 2018).

Luce, H., Kantha, L., Hashiguchi, H., Lawrence, D., & Doddi, A. (2018). Turbulence kinetic energy dissipation rates estimated from concurrent UAV and MU radar measurements. *Earth Planets and Space, 70*(1), 207–236.

Mettler, B., Dadkhah, N., & Kong, Z. (2010). Agile autonomous guidance using spatial value functions. *Journal of Control Engineering Practice, 18*(7), 773–788.

Mettler, B., Kong, Z., Goerzen, C., & Whalley, M. (2014). Guidance performance benchmarking for autonomous rotorcraft. *Journal of the American Helicopter Society, 59*(4), 1–16.

Milluzzo, J., & Leishman, G. (2010). Assessment of rotorcraft brownout severity in terms of rotor design parameters. *Journal of the American Helicopter Society, 55*(3), 32009–32009.

Miyahara, M. (1993). Utilization of helicopter for agriculture in Japan. *Weed & Turfgrass Science, 13*, 185–194.

Nansen, C., & Elliot, N. (2016). Remote sensing and reflectance profiling in entomology. *Annual Review of Entomology, 61*, 139–158.

Parabug. (2018). Parabug. https://www.parabug.solutions/. (Accessed 7 October 2018).

Pearl, E. (2015, April 20). *Drone used to drop beneficial bugs on corn crop.* Australia: The University of Queensland. News (UQ News). Retrieved from https://www.uq.edu.au/news/.

Pederi, Y. A., & Cheporniuk, H. S. (2015). Unmanned aerial vehicles and new technological methods of monitoring and crop protection in precision agriculture. In *IEEE 3rd International Conference Actual Problems of Unmanned Aerial Vehicles Developments Proceedings* (pp. 298–301).

Qin, W., Qiu, B., Xue, X., Chen, C., Xu, Z., & Zhou, Q. (2016). Droplet deposition and control effect of insecticides sprayed with an unmanned aerial vehicle against plant hoppers. *Crop Protection, 85*, 79–88.

Qin, W., Xue, X., Zhou, L., Zhang, S., Sun, Z., Kong, W., et al. (2014). Effects of spraying parameters of unmanned aerial vehicle on droplets deposition distribution of maize canopies. *Transactions of the Chinese Society of Agricultural Engineering, 30*(5), 50–56.

Rokhmana, C. A. (2015). The potential of UAV-based remote sensing for supporting precision agriculture in Indonesia. *Procedia Environmental Sciences, 24*, 245–253.

Ru, Y., Zhou, H., Fan, Q., & Wu, X. (2011). *Design and investigation of ultra-low volume centrifugal spraying system on aerial plant protection.* American Society of Agricultural and Biological Engineers, 2011 Louisville, KY, August 7-10, 2011.

Sato, A. (2003). *The RMAX helicopter UAV.* Shizuoka, Japan: Report of the Aeronautic Operations Yamaha Motor CO., LTD.

Shim, D. H., Han, J. S., & Yeo, H. T. (2009). A development of unmanned helicopters for industrial applications. *Journal of Intelligent and Robotic Systems, 54,* 407—421.

Sparks, T. C., & Nauen, R. (2015). IRAC: Mode of action classification and insecticide resistance management. *Pesticide Biochemistry and Physiology, 121,* 122—128.

Stull, R. B. (2012). *An introduction to boundary layer meteorology.* Springer Science & Business Media.

Van Leeuwen, T., Vontas, J., Tsagkarakou, A., Dermauw, W., & Tirry, L. (2010). Acaricide resistance mechanisms in the two-spotted spider mite tetranychus urticae and other important Acari: A review. *Insect Biochemistry and Molecular Biology, 40,* 563—572.

Wood, B., & Henry, A. (2011). *Wiley-blackwell encyclopedia of human evolution.* West Sussex, UK: John Wiley & Sons, Ltd.

Xiongkui, H., Bonds, J., Herbst, A., & Langenakens, J. (2017). Recent development of unmanned aerial vehicle for plant protection in East Asia. *International Journal of Agricultural and Biological Engineering, 10,* 18—30.

Xue, X., Lan, Y., Sun, Z., Chang, C., & Hoffmann, W. C. (2016). Develop an unmanned aerial vehicle based automatic aerial spraying system. *Computers and Electronics in Agriculture, 128,* 58—66.

Yun, G., Mazur, M., & Pederii, Y. (2017). Role of unmanned aerial vehicles in precision farming. In *Proceedings of the National Aviation University* (pp. 106—112). N1.